

5 **Juno Spacecraft Measurements of Jupiter’s Gravity Imply a Dilute Core**

6 BURKHARD MILITZER,^{1,2} WILLIAM B. HUBBARD,³ SEAN WAHL,¹ JONATHAN I. LUNINE,⁴ ELI GALANTI,⁵ YOHAI KASPI,⁵
7 YAMILA MIGUEL,^{6,7} TRISTAN GUILLOT,⁸ KIMBERLY M. MOORE,⁹ MARZIA PARISI,¹⁰ JOHN E.P. CONNERNEY,^{11,12}
8 RAVID HELLED,¹³ HAO CAO,¹⁴ CHRISTOPHER MANKOVICH,⁹ DAVID J. STEVENSON,⁹ RYAN S. PARK,¹⁰ MIKE WONG,^{15,16}
9 SUSHIL K. ATREYA,¹⁷ JOHN ANDERSON,¹⁰ AND SCOTT J. BOLTON¹⁸

10 ¹*Department of Earth and Planetary Science, University of California, Berkeley, CA, 94720, USA*

11 ²*Department of Astronomy, University of California, Berkeley, CA, 94720, USA*

12 ³*Lunar and Planetary Laboratory, University of Arizona, Tucson, AZ 85721, USA*

13 ⁴*Department of Astronomy, Cornell University, Ithaca, NY 14853, USA*

14 ⁵*Department of Earth and Planetary Sciences, Weizmann Institute of Science, Rehovot 76100, Israel*

15 ⁶*SRON Netherlands Institute for Space Research, Sorbonnelaan 2, NL-3584 CA Utrecht, The Netherlands*

16 ⁷*Leiden Observatory, University of Leiden, Niels Bohrweg 2, 2333 CA Leiden, The Netherlands*

17 ⁸*Universite Cote d Azur, OCA, Lagrange CNRS, 06304 Nice, France*

18 ⁹*Division of Geological and Planetary Sciences, California Institute of Technology, Pasadena, California 91125, USA*

19 ¹⁰*Jet Propulsion Laboratory, 4800 Oak Grove Dr., Pasadena, CA 91011, USA*

20 ¹¹*Space Research Corporation, Annapolis, MD 21403, USA*

21 ¹²*NASA Goddard Space Flight Center, Greenbelt, MD 20771, USA*

22 ¹³*Institute for Computational Science, University of Zurich, Winterthurerstr. 190, CH-8057 Zurich, Switzerland*

23 ¹⁴*Department of Earth and Planetary Sciences, Harvard University, 20 Oxford Street, Cambridge, MA 02138, USA*

24 ¹⁵*Center for Integrative Planetary Science, University of California, Berkeley CA 94720, USA*

25 ¹⁶*SETI Institute, 189 Bernardo Ave 200, Mountain View, CA 94043, USA*

26 ¹⁷*University of Michigan, Climate and Space Sciences and Engineering, Ann Arbor, MI 48109, USA*

27 ¹⁸*Southwest Research Institute, San Antonio, TX 78238, USA*

28 **ABSTRACT**

29 The Juno spacecraft measured Jupiter’s gravity field and determined the even and odd zonal harmonics, J_n , with unprecedented precision. However, interpreting these observations has been a challenge because it is difficult to reconcile the unexpectedly small magnitudes of the moments J_4 and J_6 with conventional interior models that assume a large, distinct core of rock and ice. Here we show that the entire set of gravity harmonics can be matched with models that assume an *ab initio* equation of state, wind profiles, and a dilute core of heavy elements that are distributed as far out as 63% of the planet’s radius. In the core region, heavy elements are predicted to be distributed uniformly and make up only 18% by mass because of dilution with hydrogen and helium. Our models are consistent with the existence of primary and secondary dynamo layers that will help explain the complexity of the observed magnetic field.

39 *Keywords:* giant planets, Jupiter interior model, gravity science, dilute core

40 **1. INTRODUCTION**

41 Conventional models for giant planet interiors are constructed with a compact core of rock and ice and atop which is a hydrogen-helium envelope. Since hydrogen and helium are predicted to become immiscible at megabar pressures (Stevenson & Salpeter 1977), one typically separates this envelope into an upper helium-depleted layer of molecular hydrogen, an intermediate helium rain layer, and a deep helium-enriched layer of metallic hydrogen. There is indeed good evidence that helium rain has occurred in Jupiter because the *Galileo* entry probe measured a helium

46 mass fraction of $\tilde{Y} \equiv Y/(X + Y) = 0.238 \pm 0.005$ (von Zahn et al. 1998) that is well below the protosolar value of
 47 0.2777 (Lodders 2010). Furthermore, neon in Jupiter’s atmosphere was measured to be nine-fold depleted relative to
 48 solar, and this can be attributed to efficient dissolution in helium droplets (Roulston & Stevenson 1995; Wilson &
 49 Militzer 2010). However, many details of layering in giant planet interiors have remained uncertain. Since a detailed
 50 experimental characterization of H-He phase separation is still outstanding, one relies instead on predictions from *ab*
 51 *initio* computer simulations (Morales et al. 2013) to constrain the thickness of the helium rain layer. Also, the abun-
 52 dance of elements heavier than hydrogen and helium is poorly constrained in all but the uppermost layer of Jupiter’s
 53 atmosphere. The *Galileo* entry probe measured the heavy element abundances up to a pressure of 22 bars. There,
 54 noble gases and several other heavy elements were found to have approximately three times the protosolar concen-
 55 tration (Mahaffy et al. 2000; Wong et al. 2004). In contrast, the probe measured sub-solar concentrations of oxygen,
 56 the element with the largest mass contribution due its high relative solar abundance. Prior to *Juno*, it was debated
 57 whether the sub-solar oxygen is representative of the average envelope, or if it reflects inhomogeneities associated with
 58 dynamical processes localized to the five-micron hotspot into which the probe fell.

59 The *Juno* spacecraft, in orbit about Jupiter since 2016, improved our knowledge of the gravity field through multiple
 60 close flybys. These measurements are summarized in terms of zonal gravity coefficients, J_n , which are integrals over
 61 all mass,

$$J_n = -\frac{2\pi}{Ma^n} \int_{-1}^{+1} d\mu \int_0^{r_{\max}(\mu)} dr r^{n+2} P_n(\mu) \rho(r, \mu) \quad , \quad (1)$$

62 where M and a are the planet’s mass and equatorial radius. P_n are the Legendre polynomials and ρ represents the
 63 planet’s density at radius r and colatitude θ with $\mu = \cos \theta$. Throughout this work, we use $GM = 1.266865341 \times 10^{17}$
 64 km^3s^{-2} from Durante et al. (2020), a 1 bar radius of $a = 71492$ km from (Lindal et al. 1981) and a rotation period of
 65 9:55:29.711 hours or $870.536^\circ/\text{day}$ from Archinal et al. (2010). The dimensionless rotational parameter then becomes
 66 $q_{\text{rot}} = \frac{\Omega^2 a^3}{GM} = 0.08919543238$.

67 Matching the *Juno* measurements (Durante et al. 2020) in Tab. 1 with conventional interior models has been a
 68 challenge. Models typically predict values for J_4 and J_6 that are larger in magnitude than was measured, as illustrated
 69 in Fig. 1. This discrepancy has made it difficult to draw conclusions from the gravity measurements about Jupiter’s
 70 interior structure and evolution. Earlier work has demonstrated that it is possible to bridge the J_4 - J_6 discrepancy by
 71 *reducing the density* of hydrogen, helium and heavy elements in the planet’s interior in a number of ways. One can,
 72 e.g., assume a subsolar value of the heavy element fraction, Z_1 (Hubbard & Militzer 2016; Wahl et al. 2017). [For the
 73 heavy element abundance of the protosolar nebula, we assume the value of $Z_{\text{solar}} = 0.0153$ from the composition model
 74 of Lodders (2010).] One can also make the interior hotter by raising the interior entropy (Wahl et al. 2017) but the
 75 resulting models are no longer compatible with the adiabatic temperature profile starting from $T_{1\text{bar}} = 166.1$ K that
 76 the *Galileo* probe measured (Seiff et al. 1997). Nettelmann et al. (2012) showed that one can also reduce the density
 77 in the deep interior by adopting an equation of state (EOS) that has a different entropy than is predicted by *ab initio*
 78 simulations (Militzer & Hubbard 2013). Different EOSs and 1 bar temperatures higher than 166.1 K were recently
 79 employed by Miguel et al. (2022) to demonstrate that the heavy element abundance cannot be constant throughout
 80 Jupiter’s envelope.

81 Recently Debras et al. (2021) proposed that the density in Jupiter’s deep interior could be reduced by invoking
 82 a stably stratified layer at intermediate pressures. To match the *Juno* gravity data, such models assume that the
 83 temperature profile of a deep adiabat of composition $Z > Z_{\text{solar}}$ is higher and its density is lower than an adiabat with
 84 $Z \approx Z_{\text{solar}}$. So far, this assumption is not supported by experiments or *ab initio* simulations (Soubiran & Militzer
 85 2015). Earlier Debras & Chabrier (2018) addressed the J_4 - J_6 challenge by reducing the density in an intermediate
 86 layer from ~ 1 to 5 Mbar by adopting a higher entropy (or temperature) and/or a subsolar heavy element abundance.

87 In this article, we match J_4 and J_6 by adopting a dilute core that extends to $\sim 63\%$ of the planet’s radius. It makes
 88 the density in the deep envelope *more dense* than in models that assume a compact core. We explain why a dilute
 89 core allows us to match J_4 and J_6 . Here *dilute core* refers to a still evolving state in which the Z component has been
 90 dissolved and greatly diluted into a hydrogen-rich envelope. Wahl et al. (2017) showed already that approximately
 91 one third of the J_4 - J_6 discrepancy can be ameliorated by assuming Jupiter has a dilute core. Here we develop this
 92 approach further by combining assumptions for the planet’s interior and with models for winds. We optimize model
 93 parameters for the interior and for winds simultaneously, which enables us to match the entire set of even and odd
 94 gravity harmonics under one selfconsistent set of assumptions.

Table 1. Comparison of *Juno* measurements (Durante et al. 2020) and predictions of model A for the even and odd gravity coefficients. Interior and wind models both make contributions to the even J_n while for the odd J_n , only the wind contributions matter. Results of wind model (i) are shown. With wind approach (ii), the *Juno* measurements can be matched to 4 significant digits.

Even $J_n \times 10^6$	J_2	J_4	J_6	J_8	J_{10}
Interior model	14696.4484	-586.8463	34.4692	-2.4983	0.2067
Wind model (i)	0.0579	0.2377	-0.2684	0.0763	-0.0231
Interior+wind	14696.5063	-586.6086	34.2008	-2.4220	0.1837
<i>Juno</i> measurement	14696.5063	-586.6085	34.2007	-2.422	0.181
3- σ error bar	0.0017	0.0024	0.0067	0.021	0.065
Deviation model-measur.	0.0000	-0.0001	0.0001	0.0000	0.0027
Odd $J_n \times 10^6$	J_3	J_5	J_7	J_9	
Wind model (i)	-0.0569	-0.0750	0.1354	-0.1157	
<i>Juno</i> measurement	-0.0450	-0.0723	0.120	-0.113	
3- σ error bar	0.0033	0.0042	0.012	0.036	
Deviation model-measur.	-0.0119	0.0027	0.015	0.003	

NOTE—Machine readable data files for model A are included in the supplemental material.

95 Our results differ from predictions in a recent paper on Jupiter’s interior by Nettelmann et al. (2021). This paper
 96 does not model the effects of winds on zonal harmonics and does not use our optimization procedure to find models
 97 consistent with given EOS, but rather modifies the EOS to obtain a match with the *Juno* data. Nettelmann et al. (2021)
 98 compute zonal harmonics using a seventh-order theory of figures, which brings the predictions in better agreement
 99 with CMS results than earlier lower-order calculations. With knowledge of the predictions in this article, Idini &
 100 Stevenson (2022) recently invoked a dilute core to relate large values of the tidal Love number k_{42} to internal waves
 101 that are trapped in the core.

102 2. METHODS AND MODEL ASSUMPTIONS

103 All interior models are derived with the concentric MacLaurin spheroid (CMS) method (Hubbard 2013; Militzer
 104 et al. 2019) with 1025 or 2049 spheroids that enables one to model a rotating planet in hydrostatic equilibrium without
 105 invoking perturbative methods. For given pressure and entropy, the density of the mixture of hydrogen, helium, and
 106 heavier elements is obtained by combining the equations of states of Saumon et al. (1995) at low pressure with the *ab*
 107 *initio* results (Militzer 2013; Militzer & Hubbard 2013) at high pressure. Heavy elements are incorporated according
 108 to Hubbard & Militzer (2016).

109 In this article, we report results from models of types A, B, and I that invoke slightly differing assumptions for
 110 the interior but all rely on a dilute core and a core transition layer where the heavy element abundance, $Z(P)$,
 111 changes (see Fig. 2). In model A, we keep hydrogen-helium mass ratio constant as $Z(P)$ changes across this layer,
 112 $\tilde{Y} \equiv Y/(X+Y) = \text{constant}$. In our initial models of type I, we kept the helium mass fraction Y instead of \tilde{Y} constant
 113 across the core transition layer. The impact on the compute gravity field is small but we consider keeping \tilde{Y} constant
 114 to be more plausible because the hydrogen-helium ratio probably remained constant as heavy elements were added to
 115 this layer. The other difference between models A and I is that in models I, we represent the heavy element abundance
 116 by a flexible piecewise linear function of $\log(P)$ with 11 knots. As we learned that so much flexibility was not needed,
 117 we constructed models of type A for which we assume the heavy element abundance is constant at low pressure, Z_1 ,
 118 as well as at high pressure inside the dilute core, Z_2 . It changes linearly between these two values across the core
 119 transition layer (see Fig. 2). In Tab. 1, we summarize all the parameters and provide values for a reference model of
 120 type A. For models of type B, we make the same assumptions as for A models but we change the equation of state
 121 for hydrogen-helium mixtures over selected pressure intervals (see Tab. 3) in order to determine the impact on the
 122 inferred heavy element abundance.

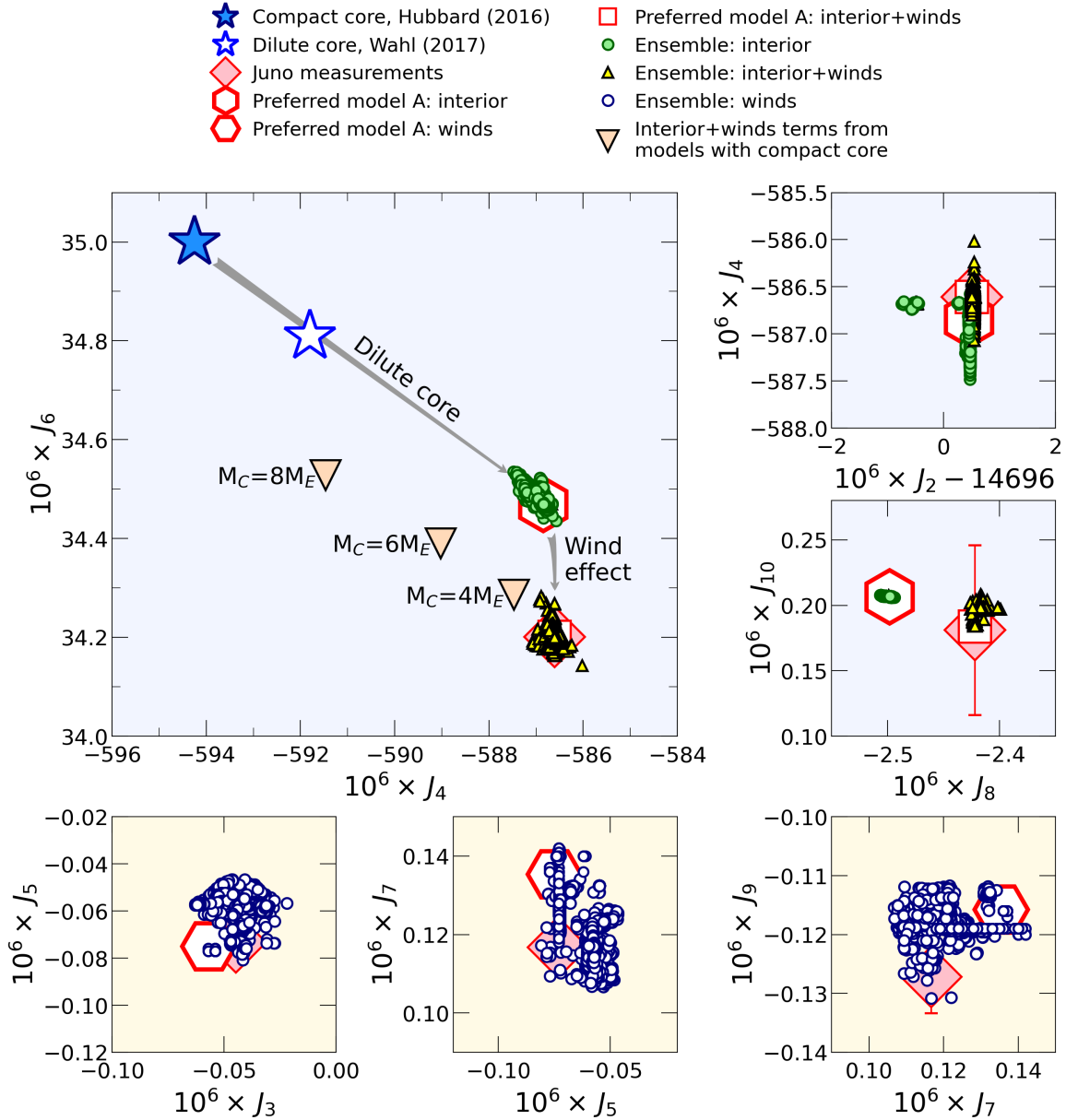


Figure 1. Comparison of *Juno* measurements (diamonds) and model predictions for the even and odd gravity coefficients. The large open symbols show results from the dilute core model A in Tab. 1 while the small symbols represent ensembles of A- and I-type models. The stars show earlier model predictions from Hubbard & Militzer (2016) and Wahl et al. (2017). The large triangles show models that combine dilute and compact cores. The labels indicate the masses of their compact cores in Earth masses.

123 We assume Jupiter’s outer molecular layer to be homogeneous and convective. Its entropy, S_1 , is set to match
 124 $T_{1\text{bar}} = 166.1$ K. Its helium mass fraction, Y_1 , is set to match the observed value of $Y/(X + Y) = 0.238$. The only
 125 adjustable parameter in this layer is the heavy element fraction, Z_1 . We introduce two pressures, $P_{\text{rain},1}$ and $P_{\text{rain},2}$,
 126 that mark the boundaries of the helium rain layer. Following Militzer et al. (2019) their values are adjustable but
 127 constrained to remain close to the predictions of the *ab initio* simulations by Morales et al. (2013) so that the entropy
 128 S_2 is constrained to be between S_1 and a maximum entropy consistent with helium immiscibility curve. Throughout
 129 this helium rain layer, we gradually change the entropy as well as the helium fraction between value of the layers above
 130 and below.

Table 2. Description of model parameters and values in our preferred model A.

Parameter	Value in model A	Description
S_1 ($k_B/\text{el.}$)	7.078	Entropy in the outer molecular layer. Fixed to match the temperature at 1 bar of 166.1 K in all models.
Z_1	0.0156	Adjustable parameter that represents the mass fraction of heavy elements in the molecular layer. A penalty is added to models with $Z_1 < Z_{\text{solar}}$.
Y_1	0.2332	Helium mass fraction in outer layer. Fixed to match the observed value of $Y_1/(1 - Z_1) = 0.238$.
$P_{\text{rain},1}$ (GPa)	93.1	Adjustable parameter for the starting pressure of the helium rain layer. The corresponding temperature, T_1 , follows from S_1 and the EOS. As explained in Militzer et al. (2019), a penalty is introduced if $P_{\text{rain},1}$ and T_1 deviate from the H-He immiscibility curve of Morales et al. (2013).
$P_{\text{rain},2}$ (GPa)	443.2	Adjustable parameter to represent the high-pressure end of helium rain layer. T_2 follows from S_2 . Again, a penalty is introduced if $P_{\text{rain},2}$ and T_2 deviate from the immiscibility curve.
α	9.4	Exponent in helium rain switching function, also an adjustable parameter.
S_2 ($k_B/\text{el.}$)	7.194	Adjustable parameter that represents the entropy in the metallic layer. It cannot exceed $7.20 k_B/\text{electron}$ to be compatible with the H-He immiscibility curve.
Y_2	...	Helium mass fraction below the helium rain layer that is constrained so that the planet overall matches the solar value of $Y/(X + Y) = 0.2777$ from Lodders (2010). Y_2 is only employed in models of type I where $Y_2(P)$ is kept constant as $Z(P)$ varies in the core transition layer.
$\tilde{Y}_2 = Y_2/(1 - Z_2)$	0.2957	Employed in models A and B so keep helium fraction $\tilde{Y}_2(P)$ below the helium rain layer constant as $Z(P)$ varies. Its value is contained so that planet overall matches solar helium fraction.
$P_{\text{core},1}$ (GPa)	784	Adjustable parameter in models A and B that marks the outer boundary in pressure of the dilute core. It affects the heavy elements according to $Z(P \leq P_{\text{core},1}) = Z_1$.
$P_{\text{core},2}$ (GPa)	2054	Adjustable parameter in models A and B that marks the inner boundary in pressure where Z of the core starts to decrease.
$Z_2(P)$...	Piecewise linear function that represents a heavy element fraction in the metallic layer. Only used in models of type I. Z_2 values is adjusted on 11 pressure points.
Z_2	0.1830	Adjustable parameter in models A and B. We set $Z(P \geq P_{\text{core},2}) = Z_2$.
w	0.1	Fractional width of the wind decay interval. Typically kept fixed at 0.1 or 0.2 but models that vary w with latitude have constructed also.

NOTE—Machine readable data files for model A are included in the supplemental material.

131 We set the helium mass fraction of the metallic layer, Y_2 , so that planet overall has a protosolar fraction of $Y/(X +$
132 $Y) = 0.2777$ (Lodders 2010). In the helium rain layer from pressure $P_{\text{rain},1}$ to $P_{\text{rain},2}$, we gradually switch from the
133 exterior adiabat of entropy S_1 and helium fraction \tilde{Y}_1 to an interior adiabat characterized by S_2 and \tilde{Y}_2 . The mass
134 fraction of heavy elements, Z_1 , remains constant. We employ the algebraic switching function,

$$f(P) = x^\alpha \quad \text{with} \quad x = \frac{\log(P/P_{\text{rain},1})}{\log(P_{\text{rain},2}/P_{\text{rain},1})} \quad , \quad (2)$$

135 to control the entropy, $S(P) = S_1 + f(P) \times (S_2 - S_1)$, and helium fraction, $\tilde{Y}(P) = \tilde{Y}_1 + f(P) \times (\tilde{Y}_2 - \tilde{Y}_1)$, at
 136 intermediate pressures. The exponent α is a positive, adjustable parameter. If it is chosen to be larger than 1, more
 137 helium has been sequestered from the upper region of the rain layer. Fig. 2 shows that models of type A favor this
 138 scenario. Conversely, if α were set to a value smaller than 1, less helium has been sequestered.

139 We employ two numerical methods to generate models that match *Juno* gravity data: the downhill simplex
 140 method (Press et al. 2001) and Markov chain Monte Carlo (MC) calculations (Goodman & Weare 2010). The cost
 141 function is dominated by the χ^2 deviation between measured values of the even and odd gravity harmonics, J_n , and
 142 the model predictions. But then we include additional penalty terms as explained in Militzer et al. (2019) that for
 143 example assure that the pressure values for the rain boundary, $P_{\text{rain},1}$ and $P_{\text{rain},2}$, are compatible with the H-He im-
 144 miscibility curve derived by Morales et al. (2013). The downhill simplex method allows to optimize a single model.
 145 The disadvantages of this method are that it tends to get stuck local minima and, more importantly, it does not
 146 provide a practical way to determine whether a minimum is global or local. This makes it difficult to decide whether
 147 model assumptions need to be modified in cases when model predictions do not match the spacecraft measurements
 148 well. Furthermore if there are degeneracies among the best models, if for example unnecessary model parameter are
 149 included, the downhill simplex will not help to identify them. MC methods on the other hand are very efficient in
 150 mapping out the allowed parameter region and in identifying parameter degeneracies. On the other hand, assessing
 151 the quality of the generated ensemble may be a challenge. For example in the MC ensemble of Guillot et al. (2018),
 152 there were models that matched the gravity data in J_4 - J_6 space. There were also models that matched in J_6 - J_8 and
 153 J_8 - J_{10} spaces but there was no model at the time that matched all J_n simultaneously. The simplex method is very
 154 good in re-optimizing selected models from the MC ensemble to assess their quality. For these reason, we combine
 155 simplex and MC methods here, which enables us provide a reference model for further use in addition to generating
 156 model ensembles.

157 2.1. Thermal wind models with latitude dependent depth

158 Kaspi et al. (2018) and Guillot et al. (2018) demonstrated that the winds on Jupiter reach to a depth of approximately
 159 3000 km. Here, we model their gravity effects by solving the thermal wind equation (Kaspi et al. 2016) for a rapidly
 160 rotating planet. We adopt the time-averaged wind profiles that were observed by tracking cloud motion (Tollefson
 161 et al. 2017) and assume they remain initially constant in the direction parallel to the planet spin axis, but then decay
 162 at some depth, H . Then we construct two ensembles of wind models under slightly different assumptions. Both
 163 fit the *Juno* data when combined with our interior models. In this section, we describe our wind approach (i) that
 164 directly employs the observed cloud-level wind profile (Tollefson et al. 2017) without modifications. Matching the even
 165 harmonics ΔJ_n requires us to make the wind depth to be latitude dependent as shown in Fig. 3. In section 2.2, we
 166 introduce our wind approach (ii) that assumes the wind depth and decay function to be independent of latitude but
 167 instead allows the wind profiles to deviate from the cloud-level observations (Fig. 3).

168 In addition to providing the J_n in Eq. (1), the CMS method also gives access to the surfaces of constant potential
 169 (gravity plus centrifugal terms) throughout the planet's interior. We use these surfaces and the density structure
 170 to solve the thermal wind equation (Kaspi et al. 2016) for a rotating, oblate planet (Cao & Stevenson 2017a) in
 171 geostrophic balance. On an equipotential surface, we construct paths, s , from the equatorial plane to the poles and
 172 integrate the dynamical part of the density, $\rho'(s)$, using

$$\frac{\partial \rho'}{\partial s} = \frac{2\Omega}{g} \frac{\partial}{\partial z} [\rho u] \quad , \quad (3)$$

173 where z is the vertical coordinate that is parallel to the axis of rotation. ρ is static background density that we derive
 174 with the CMS method. u is the differential flow velocity with respect to the uniform rotation rate, Ω , that one obtains
 175 from the planet's rotation period. g is the acceleration that we derive from the gravitational-centrifugal potential in
 176 our CMS calculations. We represent the flow field u as a product of the surface winds, u_s , and a decay function, D ,

$$u = u_s(\theta) \times D(d, H(\theta)) \quad , \quad (4)$$

177 where d presents the distance from surface and H represents the wind depth that we allow to vary between 1000 and
 178 5000 km with colatitude θ . We assume u remains initially constant but then decay to zero over a depth interval from

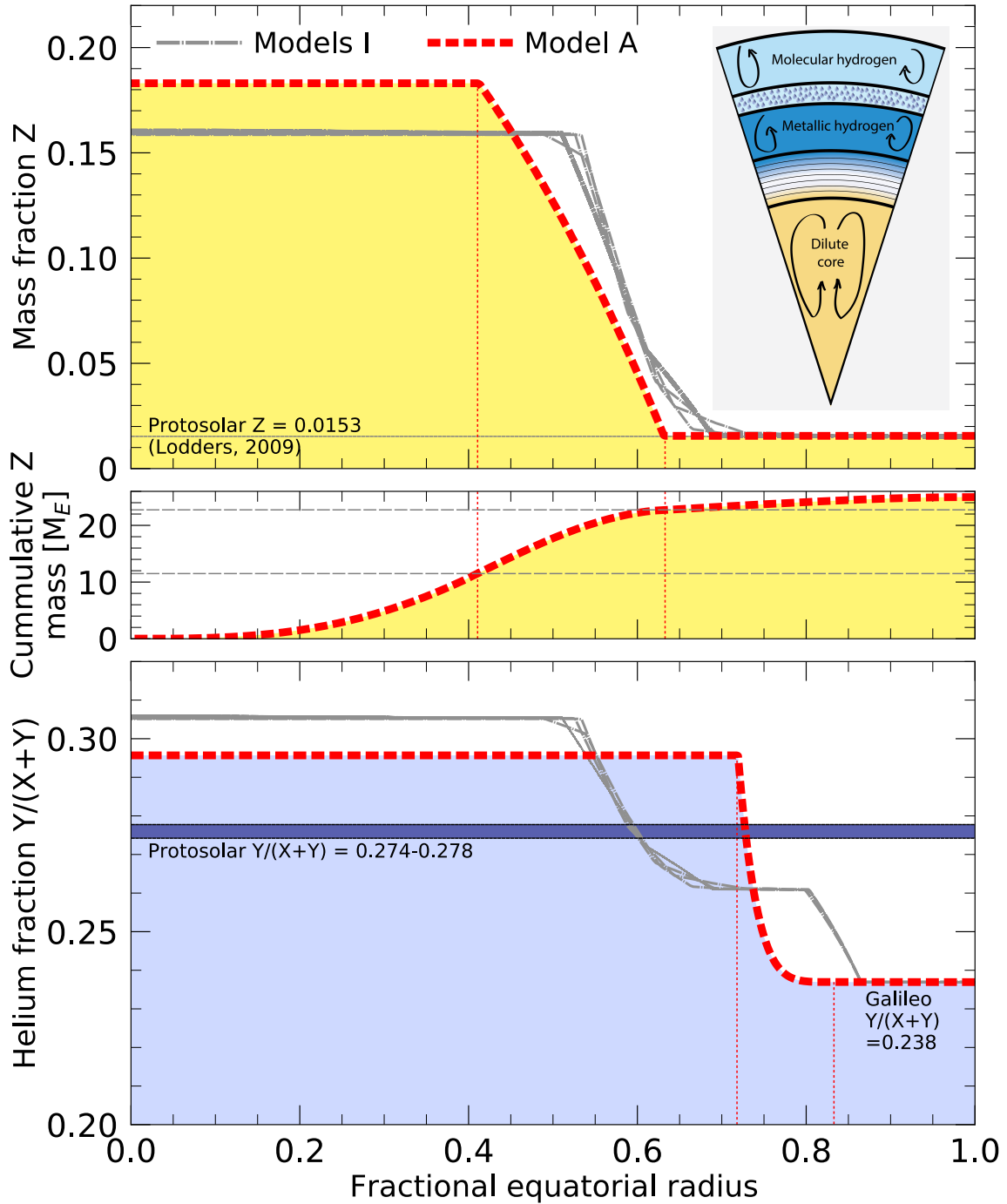


Figure 2. Predictions from models I and A for the mass fractions of heavy elements, Z , and helium, $Y/(X+Y)$, are shown as function of equatorial radius. Instead of a compact core of $Z \approx 1$, our models include a dilute core that reaches to 63% of the planet's radius ($R = 0.63$). In its inner part, the composition is uniform with Z values ranging from 0.16–0.19. This inner region is surrounded by a stably stratified layer where Z gradually decreases until it reaches a constant, approximately solar value for $R \geq 0.63$. The lower panel show the helium distribution of our models that are constrained to match measurements of the *Galileo* entry probe near $R=1$ and on average to agree with the protosolar helium abundance.

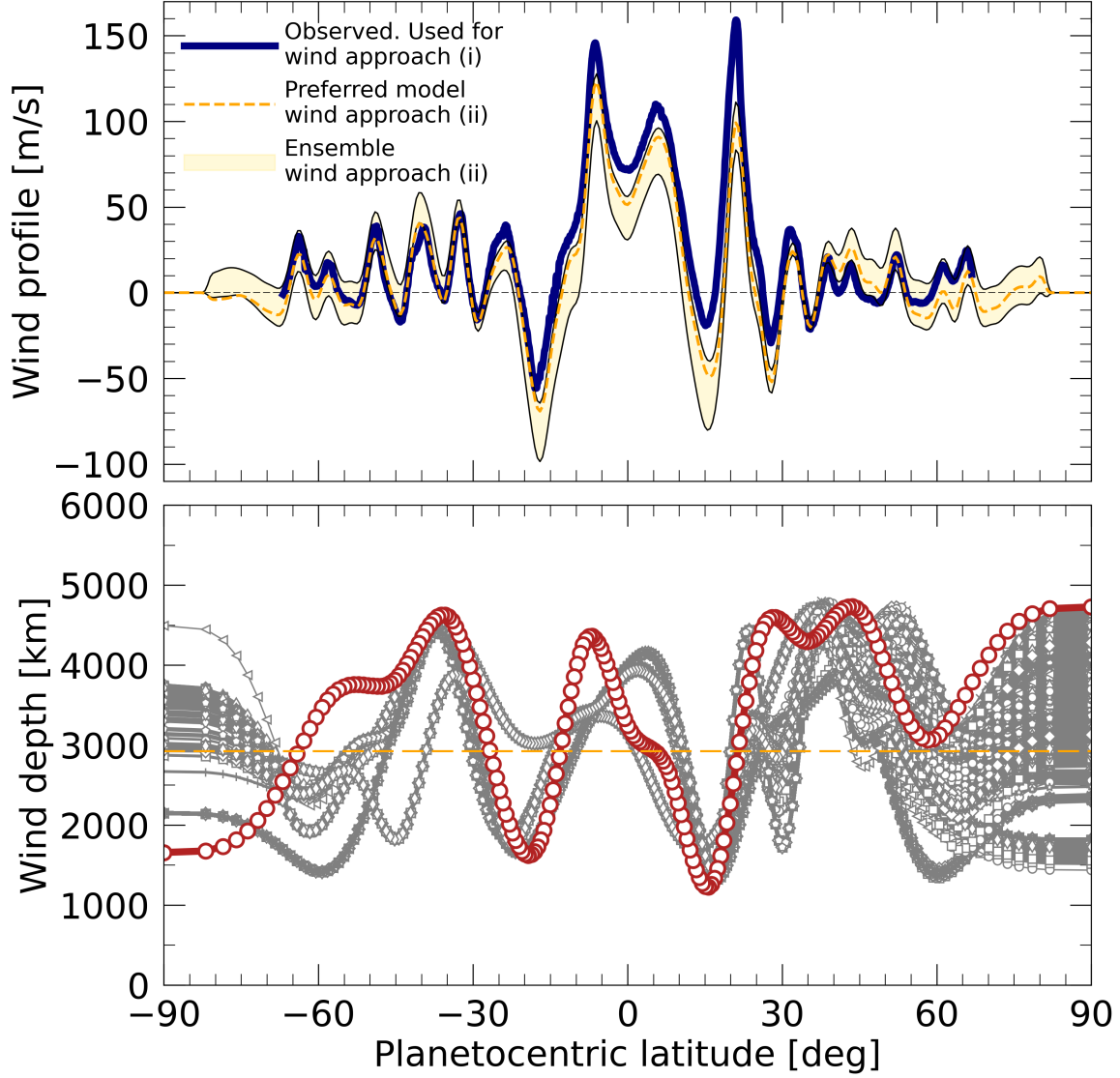


Figure 3. Winds speeds as function of latitude that were observed in Jupiter’s atmosphere (Tollefson et al. 2017). We assume they decay with depth and incorporate them into our thermal wind calculations. In our thermal wind approach (i), this wind profile is adopted without modification but the wind depth depends on latitude. The grey profiles in lower panel show an ensemble of wind depth profiles for I-type interior models. The red curve shows the wind depth profiles for our preferred interior model A. In our thermal wind approach (ii), the reconstructed cloud-level wind profiles (yellow region in upper panel) are permitted to deviate from the observations while the wind decay function is latitude independent. The dash orange curve shows wind solution for the preferred interior model A.

179 $d_1 = H[1 - w/2]$ to $d_2 = H[1 + w/2]$ according to

$$D(d, H) = D\left(x = \frac{d - d_1}{d_2 - d_1}\right) = \begin{cases} 1 & \text{for } x \leq 0 \\ \sin^2\left((1 - x)\frac{\pi}{2}\right) & \text{else} \\ 0 & \text{for } x \geq 1 \end{cases}, \quad (5)$$

180 where w is width of the decay interval. We obtain good models by setting w to 0.1 and 0.2.

181 2.2. Thermal wind model with modified cloud-level wind profiles

182 Following Kaspi et al. (2020) and Galanti & Kaspi (2021), we take the approach of allowing the cloud-level wind to
 183 be modified from the observed values. Unlike in methodology (i), in which the wind depth varies with latitude, here

184 for each solution we find an optimal wind depth and decay profile that we apply to all latitudes. For an ensemble of
 185 8752 interior models, we were able to exactly fit the odd gravity harmonics J_3 , J_5 , J_7 and J_9 and the residual even
 186 harmonics ΔJ_2 , ΔJ_4 , ΔJ_6 , ΔJ_8 and ΔJ_{10} . We start by decomposing the observed cloud-level wind profile into N
 187 Legendre polynomials, P_i ,

$$U^{\text{obs}}(\theta) = \sum_{i=0}^N A_i^{\text{obs}} P_i(\cos \theta) \quad , \quad (6)$$

188 The resulting coefficients, A_i^{obs} , represent the latitudinal shape of the observed wind profile from [Tollefson et al. \(2017\)](#).
 189 Then we introduce a second set of coefficients, A_i^{sol} , to represent a modified cloud-level wind profile,

$$U^{\text{sol}}(\theta) = \sum_{i=0}^N A_i^{\text{sol}} P_i(\cos \theta) \quad , \quad (7)$$

190 to represent solutions that may deviate from the observations. The coefficients A_i^{sol} are optimized for the wind-induced
 191 gravity harmonics to fit the spacecraft observations perfectly. We employ a very large number of polynomials, $N = 99$,
 192 so that emerging wind solution follows the observed wind profile as close as possible. The following optimization
 193 procedure ensures that the large set of coefficients are well constrained. We perform these calculations in a spherical
 194 geometry but otherwise follow the same steps as in method (i) when projecting the cloud-level winds inward, allowing
 195 it to decay in the radial direction, calculating the induced anomalous density field, and calculating the wind-induced
 196 gravity harmonics.

197 Our optimization procedure is based on the methodology of [Kaspi & Galanti \(2016\)](#) and [Galanti & Kaspi \(2021\)](#).
 198 The parameters to be optimized, i.e., those defining the depth of the wind and the cloud-level wind latitudinal profile,
 199 are defined as a control vector,

$$\mathbf{Y} = \left\{ \frac{H_0}{h_{\text{norm}}}, \mathbf{X}^{\text{sol}} \right\} \quad \text{with} \quad \mathbf{X}^{\text{sol}} = \left\{ \frac{A_0^{\text{sol}}}{u_{\text{norm}}}, \dots, \frac{A_N^{\text{sol}}}{u_{\text{norm}}} \right\} \quad , \quad (8)$$

200 where the parameter H_0 represents the radial wind depth while $h_{\text{norm}} = 10^7$ m and $u_{\text{norm}} = 10^3$ m s $^{-1}$ are the
 201 normalization factors for the depth and coefficients, respectively. The goal is to minimize the difference between the
 202 model solution and the gravity observation, and to keep the parameters from attaining unphysical values. The cost
 203 function, L , is composed of two terms

$$L = (\mathbf{J}^{\text{sol}} - \mathbf{J}^{\text{obs}}) \mathbf{W} (\mathbf{J}^{\text{sol}} - \mathbf{J}^{\text{obs}})^T + \epsilon_U (\mathbf{X}^{\text{sol}} - \mathbf{X}^{\text{obs}}) (\mathbf{X}^{\text{sol}} - \mathbf{X}^{\text{obs}})^T \quad , \quad (9)$$

204 The first is the difference between the measured and calculated gravity harmonics, and the second assures that the
 205 wind solution does not vary too far from the observed one. \mathbf{J}^{sol} is a vector that contains the model solution for J_3 ,
 206 J_5 , J_7 , J_9 , ΔJ_6 , ΔJ_8 and ΔJ_{10} while the vector \mathbf{J}^{obs} represents the corresponding measured values. The covariance
 207 matrix, \mathbf{W} , represents the uncertainties of the gravity measurements ([Durante et al. 2020](#)). We set $\epsilon_U = 5 \times 10^8$.
 208 \mathbf{X}^{obs} are the normalized observed wind coefficients. Given the value of ϵ_U and the large number of coefficients, A_i^{sol} ,
 209 the wind is strongly constrained to the observed cloud-level profile, thus ensuring that deviations from the observed
 210 values are only permitted if they result into a significant lowering of the cost function. Given an initial guess for \mathbf{Y} ,
 211 a minimal value of L is derived using the Matlab function *fmincon* ([Mathworks 2022](#)) while taking advantage of the
 212 cost function gradient that is derived from the adjoint of the dynamical model.

213 3. RESULTS AND DISCUSSION

214 Here we show that all the zonal gravity harmonics can be matched with one set of plausible assumptions, including a
 215 dilute core, a helium rain layer, and a model for the zonal wind speeds and depth. Motivated by the work of [Wahl et al.
 216 \(2017\)](#), we assume a flexible profile for the heavy element abundance in the deep interior $Z(P)$ that we represent by a
 217 piecewise linear function of $\log(P)$ (See Fig. 2). When we simultaneously optimized our interior and wind parameters
 218 under these assumptions, we found that all promising models had no or only a very small compact core. Instead, the
 219 heavy elements were distributed throughout the deep interior, extending to 63% of the planet's radius as illustrated
 220 in Fig. 2. We thus temporarily removed the compact central core from our models and extended the metallic layer to
 221 the planet's center. In section 3.2, we explain why redistributing mass from the compact core reduces the magnitude
 222 of J_4 .

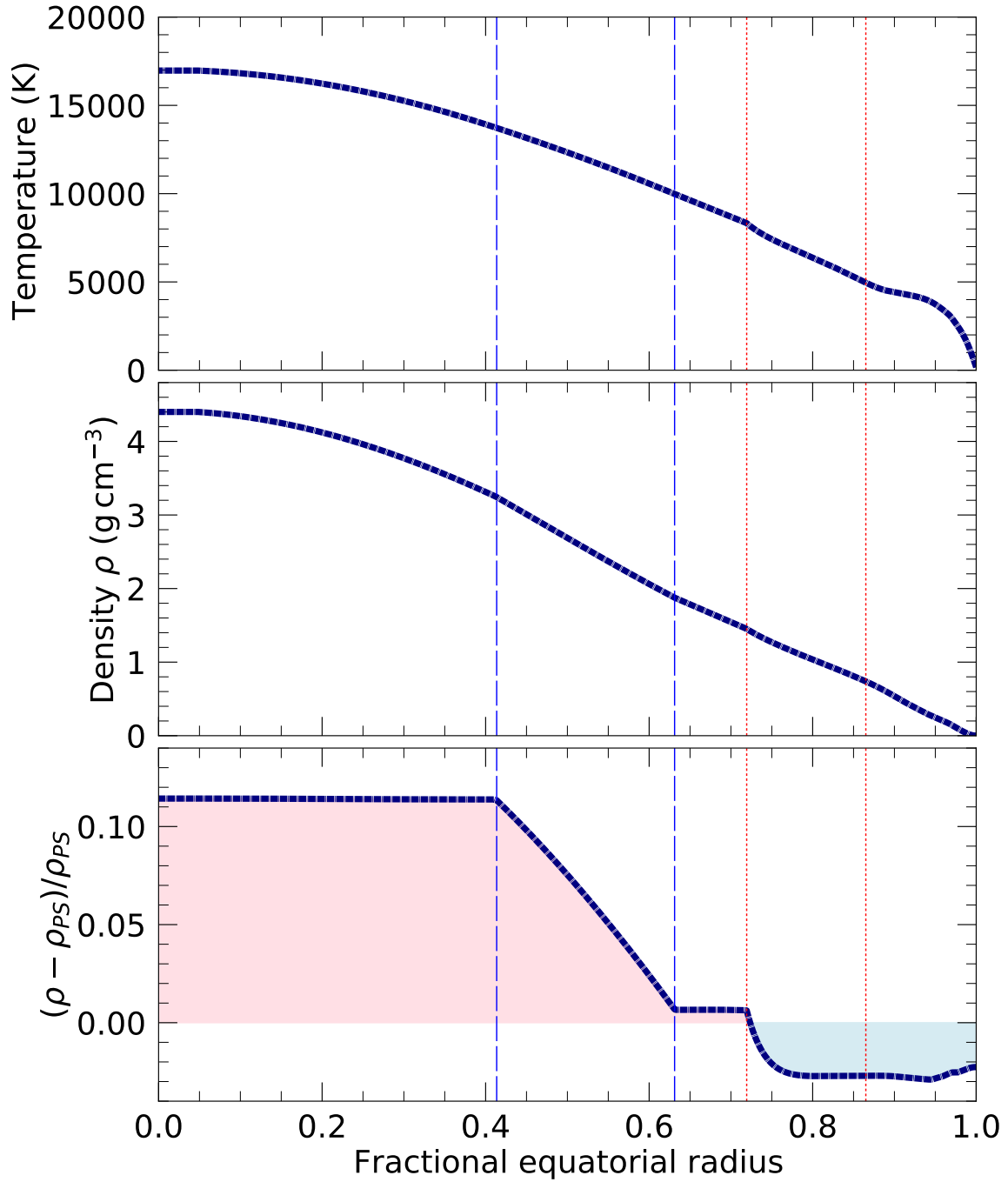


Figure 4. Temperature and density profiles to model A. The vertical dotted lines mark the boundaries of the helium rain region. The dashes lines show the boundaries of the transition layer. The lowest panel shows the density deviation from a protosolar adiabat [$Y = 0.2735$ and $Z = 0.0153$ (Lodders 2010)] for $T_{1\text{bar}} = 166.1\text{ K}$. Because of the helium sequestration, the density of model A is lower in the molecular and the helium rain layers. Conversely in the dilute core and in the core transition layer, the density of model A is much higher because of the enrichment in heavy elements. In the metallic hydrogen layer, density of model A is slightly higher than that of the protosolar adiabat because the enrichment in helium.

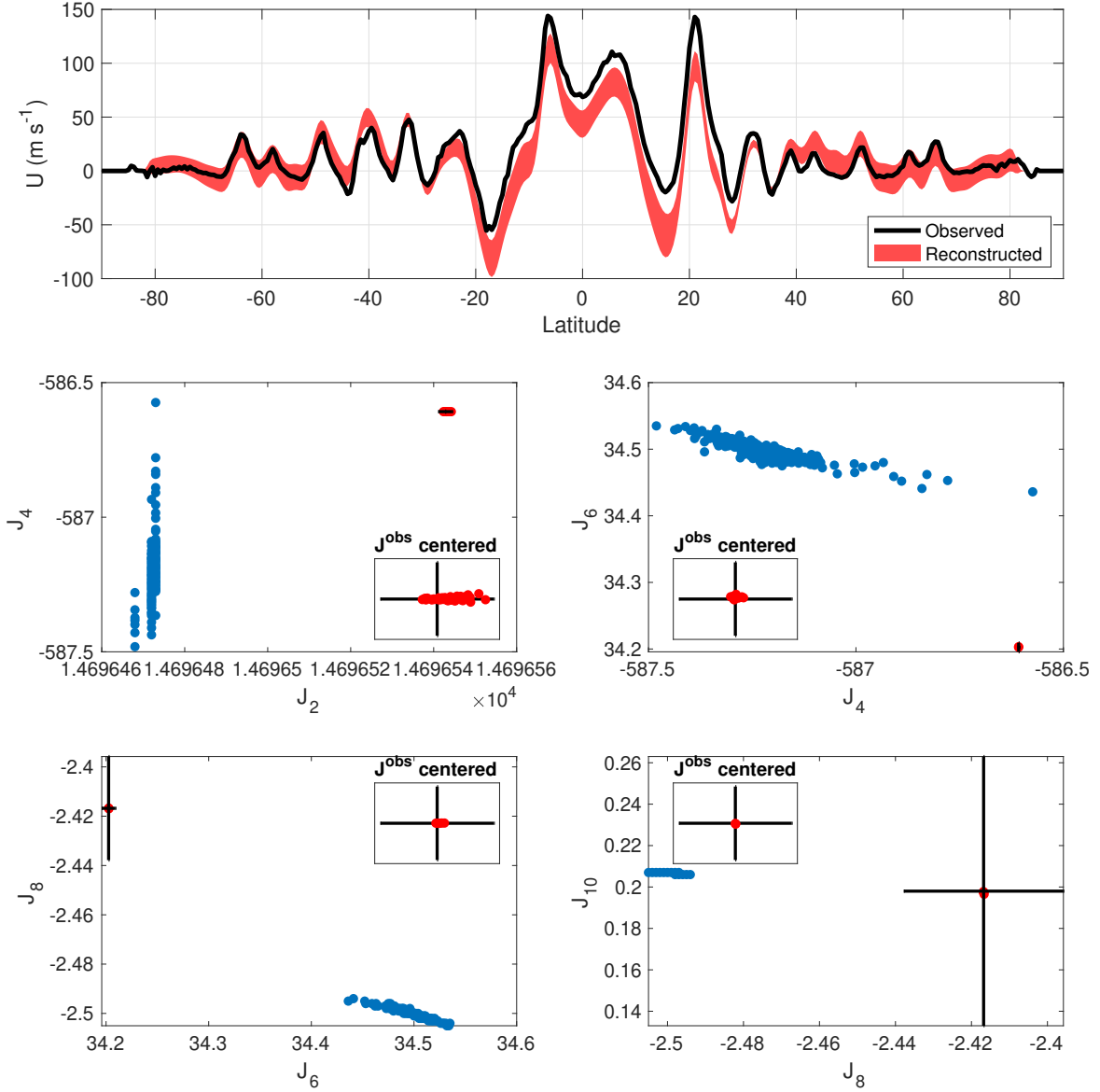


Figure 5. (a) the observed cloud-level wind (black), and the range of model solutions (red envelope) developed with thermal wind approach (ii). (b-e) the corresponding model solutions for the even gravity harmonics. Shown are the measurements (black crosses - with the size of the cross representing the measurement uncertainty), the interior model solutions (blue dots), and the model solutions when the wind-induced gravity harmonics are added to the interior model solutions (red dots). The small inserts show the zoom in on the measured values.

223 The most promising models that then emerged had a number of features in common. In the dilute core region, the
 224 abundance of heavy elements was constant. Above some radius (quantified below), it started to decay gradually until
 225 it reached the value of the outer layer, Z_1 . We consequently simplified how we represent the distribution $Z_2(P)$. We
 226 kept only two values, Z_1 and Z_2 , but introduced two pressure values $P_{\text{core},1}$ and $P_{\text{core},2}$ that mark the region of decay
 227 from Z_2 to Z_1 with decreasing pressure, as we illustrate in Fig. 2. We require this region and the helium rain layer to
 228 be Ledoux stable (Ledoux 1947). Under these assumptions, we obtained model A (see Tab. 2 and Fig. 4) whose even
 229 gravity coefficients match the *Juno* observations exceptionally well (Tab. 1). We still see some minor deviations, e.g.,
 230 for the odd gravity harmonics J_3 but the magnitude of the deviations is reasonably small but they can be eliminated
 231 with our second set of wind approach.

232 For 8572 interior models of type A that we constructed with MC calculations, we derived wind solutions with
 233 approach (ii) to match the *Juno* measurements. The resulting wind models shown in Fig. 5. Since the observed

234 wind (Tollefson et al. 2017) already allows a reasonable match to the higher gravity harmonics (Kaspi et al. 2020) only
 235 moderate modifications are needed to enable an exact fit to all the even gravity harmonics (Fig. 5a). At mid latitudes,
 236 the deviation of the optimized wind is mostly within the observed uncertainty of around 15 m s^{-1} (Tollefson et al.
 237 2017), and in the equatorial region, the deviations are larger, reaching 50 m s^{-1} . With the modified cloud-level winds,
 238 a perfect match to all gravity harmonics is reached (Fig. 5b-e). For all solutions, the depth of the wind is around
 239 3000 km.

240 In Fig. 1, we separate the contributions from our interior and wind models. Diluting the core changes interior
 241 contributions to J_4 and J_6 linearly until the residual discrepancy can be bridged with wind model that we derive
 242 self-consistently. The wind models contribute $\Delta J_4 \approx 0.24 \times 10^{-6}$ and $\Delta J_6 \approx -0.27 \times 10^{-6}$ as well as smaller amounts
 243 to all other J_n .

244 We also inserted small compact cores, composed of a 1:1 rock-ice mixture, into our dilute-core models and re-
 245 optimized all model parameters. We were able to accommodate compact cores of up to 3 Earth masses (1% of
 246 Jupiter’s mass). For larger compact cores, we cannot fit the gravity data. Already for 4 Earth masses, we find a
 247 discrepancy of $\Delta J_4 \approx 0.9 \times 10^{-6}$ [or $\sim 10^3 \sigma$ (Durante et al. 2020)] between prediction from interior models and gravity
 248 measurements that we cannot bridge with our wind model assumptions. Fig. 1 shows that for larger compact cores of
 249 up to 8 Earth masses, the gap between model predictions and the *Juno* measurements widens in J_4 - J_6 space, as mass
 250 is being moved from the dilute core region into the compact core.

251 According to model A, Jupiter has a thick, central region extending to $0.41 R_J$ that is fully convective and uniformly
 252 enriched by ~ 12 Earth masses worth of heavy elements (mass fraction 18%, see Fig. 2). Fig. 4 shows that the density
 253 of model A is higher than that of protosolar adiabat except in the outer two layers where the depletion of helium
 254 reduced it by $\sim 3\%$. Note that our dilute core solution differs from other recent Jupiter models with dilute cores that
 255 invoke compositional gradients and are stable against convection and heat is transported via conduction/radiation or
 256 semi-convection (Vazan et al. 2018; Debras & Chabrier 2019). This may imply that Jupiter’s primordial core was
 257 mixed with the envelope during a giant impact shortly after its formation (Liu et al. 2019). Analyses of the possible
 258 evolution of a primordial core show that, (a) likely constituents of the core are fully soluble in hydrogen under the
 259 relevant temperature-pressure conditions (Wahl et al. 2013; Gonzalez-Cataldo et al. 2014; Wilson & Militzer 2012a,b),
 260 and (b) the primordial core could be eroded by convective motions (Moll et al. 2017; Müller et al. 2020). The convective
 261 central region is expected to be the primary source of Jupiter’s magnetic field.

262 The core region is enveloped in a stably stratified transition layer (0.41 – $0.63 R_J$) where the heavy element abundance
 263 gradually decreases, contributing ~ 11 Earth masses of heavy elements. This layer is neither convective nor likely to be
 264 capable of generating a dynamo. Such layers might be analogous to those invoked for Saturn to explain seismological
 265 observation in its rings (Fuller 2014) and to explain the planet’s luminosity anomaly (Leconte & Chabrier 2013).

266 Atop the transition layer in Jupiter is a thin layer of metallic hydrogen (0.63 – $0.72 R_J$) that is again homogeneous and
 267 convective (inset, Fig. 2), raising the possibility of a secondary dynamo operating there. Above that is the helium rain
 268 region (0.72 – $0.83 R_J$) that would again be stably stratified. Finally the outer molecular layer is again homogeneous
 269 and convective. It only contributes ~ 2 Earth masses of heavy elements bringing total amount in the planet to ~ 25
 270 Earth masses, which is a lower bound as we discuss in section 3.3.

271 In Fig. 6, we show the inner and outer equatorial radii of the core transition region that derived from an ensemble
 272 of models that construct with the same assumption as model A. Both radii are anticorrelated so that mass of the core
 273 region is approximately preserved when these radii vary. If the outer boundary of this region is extended to larger
 274 radius, the inner boundary shrinks so that the heavy Z element abundance falls off more gradually over a larger radius
 275 interval. In Fig. 6, we also show the probability distributions of the outer and inner radii in the model ensemble.
 276 From these distributions, we derived values of 0.63 ± 0.01 and $0.41 \pm 0.03 R_J$ for both radii. The uncertainties reflect
 277 approximately 80% of the models in ensemble.

278 3.1. Dependence on the Equation of State of Hydrogen-Helium Mixtures

279 Our models of type A and I predict an approximately protosolar enrichment of $Z_1=0.0156$ for the molecular layer,
 280 apparently consistent with the lower end of the equatorial water determination at 0.7–30 bar of Li et al. (2020) between
 281 1 and 5 times solar, only if the *Galileo* determination of the carbon enrichment of 2–4 times solar (Wong et al. 2004)
 282 were not included. Assuming these two low-pressure measurements are representative for the entire molecular envelope,
 283 the carbon enrichment and $Z_1 = 0.0156$ would force the abundance of oxygen, and hence water, to be subsolar. Since

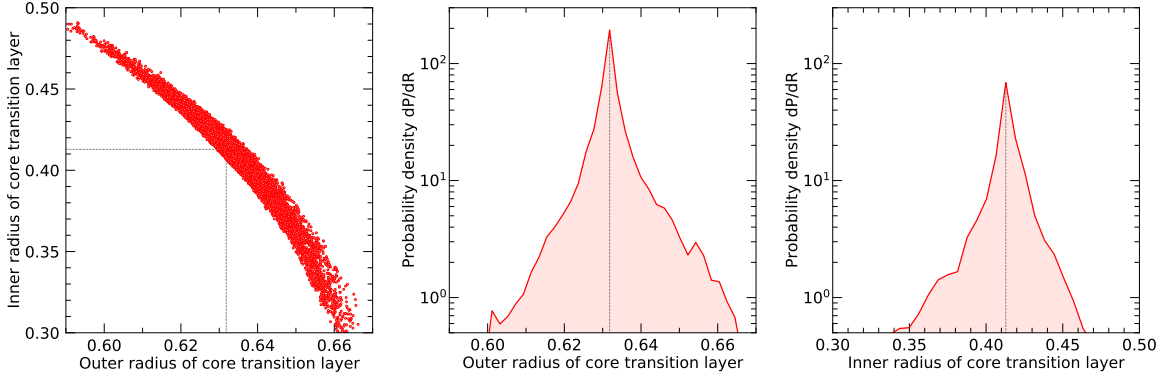


Figure 6. Inner and outer radii of the core transition layer derived from ensembles of type-A models (left panel). The probability densities in the two other panels were normalized so that integrals under the curves equal 1. For the outer and inner radii, we derived values of 0.63 ± 0.01 and 0.41 ± 0.03 respectively. The uncertainty intervals were chosen so that approximately 80% of all models are represented.

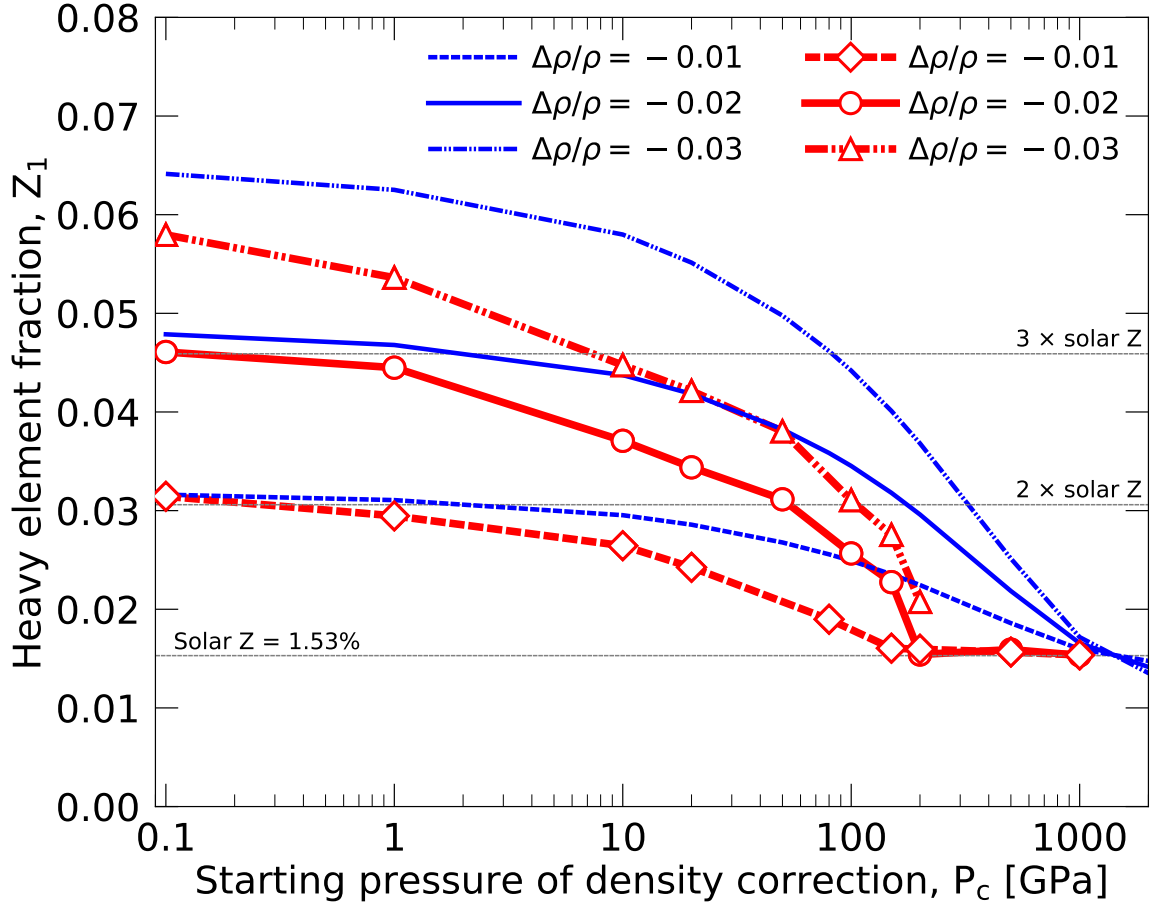


Figure 7. Model predictions for the amount of heavy elements in the molecular envelope, Z_1 , if we introduce a density correction, $\Delta\rho/\rho$, for all pressures $P \geq P_c$ to the equation of state in our A-type models and then reoptimize them to match the *Juno* measurements. The blue curves represent the results from simple reoptimizations that only match the planet's mass and J_2 . The red curves were obtained by matching the mass and all gravity coefficients, which led us to conclude that a density correction only in the metallic region for $P \geq 200$ GPa does not significantly affect Z_1 . Instead Z_1 was found to be sensitive to a density reduction in the pressure interval from 10–200 GPa.

Table 3. Model predictions for the heavy element fraction in the molecular envelope, Z_1 . In models B1–B4, the density of our H-He EOS has been lowered over the specific pressure range by a certain fraction compared to our original models A.

Model	Pressure interval	Density correction	Z_1	Z_1/Z_{solar}
type	[GPa]	$\Delta\rho/\rho$		
A	none	0	0.0156	1.00
B1	20 – 100	–0.02	0.021	1.37
B2	20 – 4500	–0.02	0.034	2.25
B3	10 – 100	–0.03	0.033	2.14
B4	10 – 4500	–0.03	0.045	2.92

so far the *Juno* spacecraft determined the water abundance only near the equator, measurements at other latitudes are warranted.

Here we probe how sensitively the predicted heavy element abundance for the molecular layer, Z_1 , depends on the hydrogen-helium equation of state that was derived with *ab initio* simulations. Models B1–B4 in Tab. 3 were derived by lowering the density by a certain fraction over the specific range of pressures.

While there are no uncertainties in the EOS at low pressure where the H-He mixture behaves like an ideal gas, it is reasonable to ask what type of EOS changes at high pressure would lead to an increase of the Z_1 values that are predicted by our models. There are uncertainties in the *ab initio* EOS (Militzer & Hubbard 2013) that was derived with density functional theory. While this is a state-of-the-art approach, an experimental confirmation is still outstanding because the uncertainties of the existing density and temperature measurements data at megabar pressures are still too large to constrain the results from *ab initio* simulations.

For any pressure and temperature, an increase in Z always increases the density. We therefore studied how our model predictions would change if the density of our H-He EOS were decreased by a fraction of 1, 2, or 3% for all pressures above a certain threshold, P_c . We performed this analysis in two steps and report the results in Fig. 7. In the first step, we introduce the density change into model A and only match the planet and J_2 by adjusting Z_1 and Z_2 . The blue curves in Fig. 7 show a substantial increase in Z_1 even if the density is only changed for a high value of $P_c \sim 200$ GPa.

In a second step, we reoptimize the entire model with the goal of matching the planet mass and the entire set of gravity coefficients. The red curves in Fig. 7 show that a density change $P_c \geq 100$ GPa does not lead to an increase in Z_1 because in our models, the helium rain layer starts at ~ 100 GPa and thus our models are less sensitive to a density change in this layer. From these calculations, we selected models B2 and B4, which respectively incorporated a density reduction of 2% for $P_c \geq 20$ GPa and 3% for $P_c \geq 10$ GPa. The resulting Z_1 values are reported in Tab. 3.

We concluded that our models are fairly sensitive to density change in the pressure from 10 to 100 GPa. We therefore constructed two additional models B1 and B3, in which we reduced the density by 2% and 3% only in the pressure ranges from 20–100 and 10–100 GPa respectively. Under these assumptions, the heavy element abundance in the molecular layer, Z_1 , increases to 1.41 and 2.14 times the protosolar value, which is in better agreement with the noble gas and methane abundances in Jupiter’s atmosphere. To remove this uncertainty in the EOS, one would need, e.g., to conduct new laboratory experiments that measure the density of H-He mixtures to better than 2% in the pressure range 10–100 GPa while carefully controlling the temperature.

3.2. Relation of Dilute Core and J_4

There is an approximate way to understand the indirect evidence that Jupiter has an extended, low-density-contrast central region of enhanced metallicity but still dominated by hydrogen-helium, rather than a compact high-density core as had been expected prior to the *Juno* mission. Consider a traditional pre-*Juno* Jupiter model from the set published in Hubbard & Militzer (2016). For such a reference model, we select the model DFT-MD 7.13 (boldface in Table 1 in Hubbard & Militzer (2016)). For the present purpose, this model differs negligibly from the *Juno*-measured values of J_2 , M , and from the adopted equatorial radius a and rotational parameter, q_{rot} , but its predicted $J_4 = -596.05 \times 10^{-6}$

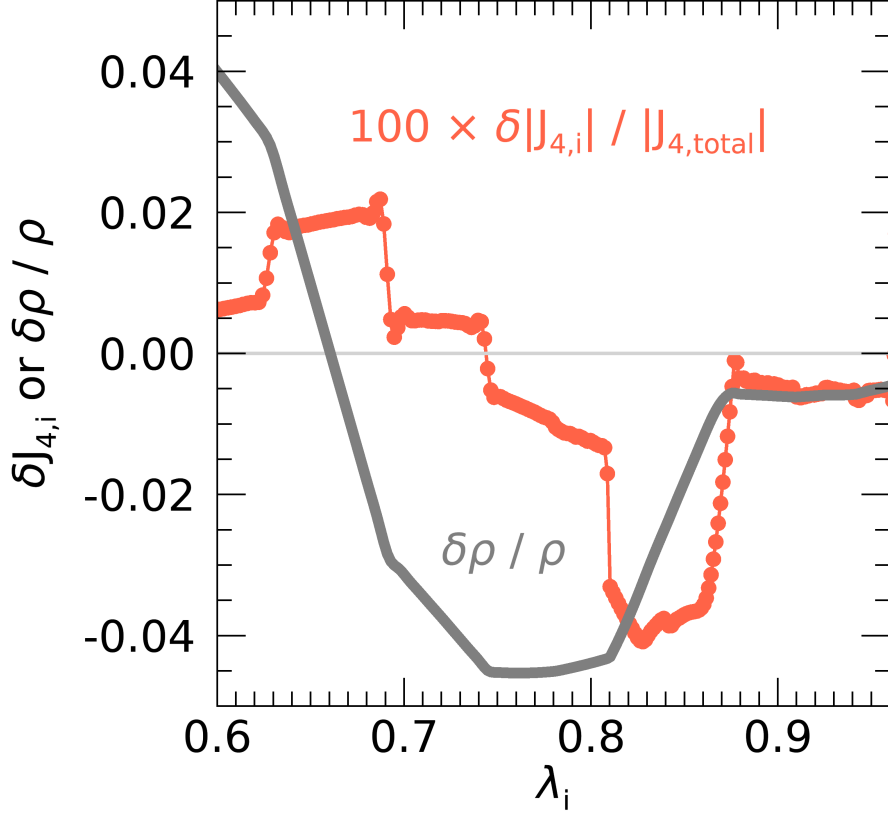


Figure 8. Density modification and corresponding correction to J_4 is shown as function equatorial spheroid radius λ_i .

320 is 1.6% larger in absolute value than the *Juno* measurement. We will refer to this 2016 Jupiter model as PJM (for
 321 Preliminary Jupiter Model). The PJM has a high-density central core of $12.2 M_E$ with a radius of $0.15 a$.

322 Here we report a Jupiter interior model that fits all the *Juno* gravitational constraints including J_4 . Because Jupiter's
 323 interior structure approximately resembles a polytrope of index one, we can use a perturbation approach to examine
 324 the effect of a small density modification on the predicted J_4 . This is possible because unlike J_2 , the zonal harmonic
 325 J_4 and all higher zonal harmonics (in the absence of wind corrections) are excited by higher-order responses to q_{rot} .
 326 Accordingly, Hubbard (1974) derives, for a polytrope-like planet, the approximate relation

$$J_4 \approx -\frac{4\pi}{35} \left[J_2 + \frac{1}{3} q_{\text{rot}} \right] \frac{b^3}{M} \rho(b) \quad , \quad (10)$$

327 where b is the planet's polar radius, and the density $\rho(b)$ is evaluated on a level surface whose mean radius is b ,
 328 corresponding to a CMS value of about $\lambda \approx 0.93$ (corresponding to a pressure of about 20 GPa in Jupiter's interior).
 329 As argued by Hubbard, the density distribution deeper in the polytrope-like planet contributes little to the total
 330 external value of J_4 .

331 Define $\delta J_4 = J_4 - J_4^{\text{PJM}}$, where J_4 is the value for the present optimized model, fitted to the *Juno* measurement,
 332 and $J_4^{\text{PJM}} = -596.05 \times 10^{-6}$. Similarly, let $\delta \rho = \rho - \rho^{\text{PJM}}$, evaluated at $\lambda \approx 0.93$. Using Eq. 10, and holding J_2 , M ,
 333 q_{rot} , and b constant, we get

$$\frac{\delta J_4}{J_4} \approx \frac{\delta \rho_4}{\rho_4} \quad (11)$$

334 where ρ and $\delta \rho$ are evaluated around $\lambda \approx 0.93$. Recognizing that Eqs. 10 and 11 are crude approximations, they
 335 correctly show the order of magnitude of the decrease of $|J_4|$ due to negative $\delta \rho = \rho - \rho_{\text{PJM}}$. Fig. 8 shows a detailed
 336 comparison of the present optimized Jupiter model with the PJM.

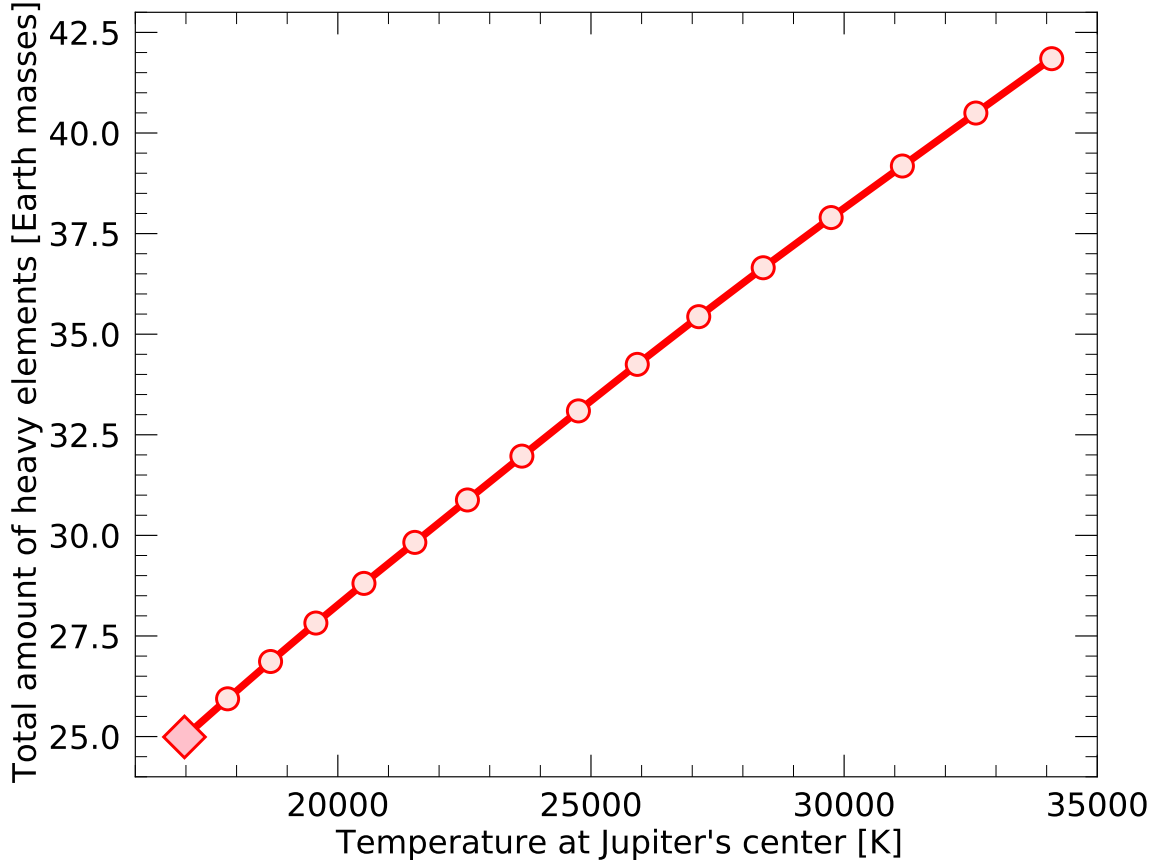


Figure 9. If one assumes a superadiabatic temperature gradient (circles) in the stably stratified transition layer ($0.41\text{--}0.63 R_J$) one can construct interior models that accommodate a larger amount of heavy elements (Y axis) than in model A (diamond symbol) because the temperature in the core region is higher. We represent this temperature change by plotting against the temperature in the planet’s center (X axis).

337 A literal application of Eq. 11 to the layer at the equatorial radius of $\lambda \approx 0.93$ would predict $\delta\rho/\rho \approx -0.016$, about
 338 three times larger than the grey curve in this region, but the sign and order of magnitude is correct. The bulk of the
 339 downward shift in $|J_4|$ arises from spheroids between $\lambda \approx 0.75$ and $\lambda \approx 0.96$; a smaller upward contribution comes
 340 from spheroids between $\lambda \approx 0.75$ and $\lambda \approx 0.6$. There is no significant contribution to $|J_4|$ from deeper layers.

341 As we see from Fig. 8, J_4 is fitted by shifting the density downward by 1 to 4% in the outer layers of Jupiter. Once
 342 we have done this, we must readjust layers for $\lambda < 0.6$ in order to maintain constant the values of J_2 and M . With
 343 the possible exception of extreme, unrealistic interior models, there is a correlation between J_2 and the dimensionless
 344 moment of inertia, C/Ma^2 . Thus the value of C/Ma^2 , must be kept constant as well, always very close to 0.264.
 345 If $\delta\rho/\rho$ is negative for $\lambda > 0.65$, it must be positive for smaller values of λ . The value of M can be kept constant
 346 by inserting a small, high-density central core, but the additional requirement that C/Ma^2 be constant requires the
 347 density augmentation to be spread out to a larger central region. The effect of the starting pressure P_c for the density
 348 correction $\delta\rho/\rho$, discussed above, also can be understood in the framework of Eq. 11, since $\lambda \approx 0.93$ corresponds to
 349 about 20 GPa pressure, and $\lambda \approx 0.86$ corresponds to about 100 GPa.

350 The link between a dilute core and the increase in J_4 is also explained by models that keep Jupiter’s equatorial
 351 radius and J_2 value fixed while the density profile is arbitrarily increased over a range of pressures. Figure 5 from
 352 Guillot (1999) showed that a 5% increase in density in the 10 Mbar region yields an increase of J_4 by about 10^{-5} ,
 353 which is in line with the trend that we show in Fig. 1.

354 3.3. Superadiabatic temperature gradients in core transition layer

355 In our models, the dilute core is surrounded by stably stratified transition layer in which the heavy element abundance
 356 increases from $Z \approx 0.0156$ to 0.183. While we did not do so in model A, one might adopt a superadiabatic temperature

357 gradient for this layer (Leconte & Chabrier 2013). This would increase the temperature in the dilute core and thereby
 358 enable it to accommodate more heavy elements. We study such an increase under the following assumptions and
 359 report the resulting increase in the total Z element budget of the planet in Fig. 9.

360 While Debras & Chabrier (2019) assumed the dilute core itself to be stably stratified, we assume it to be homogeneous
 361 and convective and confine the superadiabatic temperature gradient to the core transition layer. The dilute core may
 362 then have an entropy, S_3 , that is higher than that of the metallic layer, S_2 . In the core transition layer, we interpolate
 363 the entropy linearly from S_2 to S_3 as a function of $\log(P)$ from $P_{\text{core},1}$ to $P_{\text{core},2}$,

$$S_{tr}(P) = S_2 + g(P) \times (S_3 - S_2) \geq S_2 \quad \text{with} \quad g(P) = \frac{\log(P/P_{\text{core},1})}{\log(P_{\text{core},2}/P_{\text{core},1})} \quad (12)$$

364 We employ the hydrogen-helium EOS (Militzer & Hubbard 2013) to relate the entropy to temperature before we adjust
 365 the heavy element fraction, $Z_{tr}(P)$, so that the density for a given pressure stays exactly the same as in model A,

$$\rho(S_{tr}(P), Z_{tr}(P)) = \rho(S_2, Z_A(P)) \quad \text{with} \quad Z_{tr}(P) \geq Z_A(P) + g(P) \times (Z_2 - Z_1) \quad (13)$$

366 Here entropy and heavy Z fraction trade off against each other while leaving the density unchanged. This means the
 367 gravity coefficients are the same as in model A and that the superadiabatic model is again Ledoux stable (Ledoux
 368 1947). In Fig. 9 we plot the revised total budget of heavy elements. For the simplicity, we chose the central temperature
 369 rather than the core entropy, S_3 , as X axis. We find that the planet's total heavy element contents to increase linearly
 370 with the planet's central temperature. If the central temperature doubles in magnitude, the total Z amount increases
 371 from 25.0 to 41.7 Earth masses. In this regard, our adiabatic model A represent a lower bound for the amount of the
 372 heavy elements stored in the planet. At the presenting time, we are not able to place an upper bound on the core
 373 entropy because that depends on the planet's formation and on how efficiently heat can be transported across the
 374 stably stratified layer.

4. CONCLUSIONS

375
 376 The Juno mission's measurements of Jupiter's gravity require a thorough revision of models of the interior of the solar
 377 system's largest planet. Doing so has proved to be a challenge given other constraints that must be satisfied, including
 378 atmospheric temperature and abundances of elements heavier than helium. Here we report models of Jupiter's interior
 379 that meet these constraints. Our models have a dilute core – a region substantially enriched in elements heavier –
 380 spanning 63% of the planet's radius. This unexpected feature challenges conventional models of the formation and
 381 early evolution of Jupiter.

382 Furthermore, our models have important implications for the dynamo process inside Jupiter. We predict the existence
 383 of two separate, fully convective dynamo layers inside Jupiter: the metallic layer and the dilute core, which are separated
 384 by a stably stratified layer, as shown in Fig. 2. Such a double-dynamo configuration could help explain the planet's
 385 surprisingly complex magnetic field (Connerney et al. 2018) as proposed in Moore et al. (2018). Wind activity in
 386 the bottom part of the convective molecular hydrogen layer just above the helium rain layer could further modify the
 387 observed magnetic field (Cao & Stevenson 2017b) but is unlikely to determine the main features of the magnetic field.
 388 Our interior model implies the simultaneous operation of a deep-seated, thick-shell dynamo and a shallower, thin-shell
 389 dynamo, in contrast to the homogeneous dynamo region assumed in most Jovian dynamo studies (Jones 2014; Duarte
 390 et al. 2018). The upcoming low-altitude polar passes of the *Juno* Extended Mission will map the field in the northern
 391 hemisphere with increased spatial resolution and test this hypothesis.

392 Finally, our results beg the question of how a dilute core can form inside Jupiter. Standard models of the formation
 393 of Jupiter, whether by core accretion or disk instability, do not predict such a structure (Müller et al. 2020). An
 394 obvious possibility is that a discrete primordial core was mixed with the envelope, either over a cosmic period of time
 395 by subsequent double-diffusive mixing and solution in the metallic hydrogen (Gonzalez-Cataldo et al. 2014; Moll et al.
 396 2017) or abruptly during a giant impact shortly after its formation (Liu et al. 2019). What such a catastrophic model
 397 implies for the other aspects of the Jovian system, such as the presence of four large regular satellites, are intriguing
 398 questions stimulated by Jupiter's surprising interior. Among the ways to verify predictions in this article are high
 399 pressure experiments on hydrogen, additional measurements by the *Juno* spacecraft, and Jovian seismology.

REFERENCES

- 400 Archinal, B., A'Hearn, M., Bowell, E., et al. 2010, *Celestial* 403 Cao, H., & Stevenson, D. J. 2017a, *J. Geophys. Res.*
 401 *Mechanics and Dynamical Astronomy*, 109, 404 *Planets*, 122, 686, doi: [10.1002/2017JE005272](https://doi.org/10.1002/2017JE005272)
 402 doi: [10.1007/s10569-010-9320-4](https://doi.org/10.1007/s10569-010-9320-4)

- . 2017b, *Icarus*, 296, 59–72
- Connerney, J. E. P., Kotsiaros, S., Oliverson, R. J., et al. 2018, *Geophysical Research Letters*, 45, 2590
- Debras, F., & Chabrier, G. 2018, *Astron. Astrophys.*, 609, doi: [10.1051/0004-6361/201731682](https://doi.org/10.1051/0004-6361/201731682)
- . 2019, *The Astrophysical Journal*, 872, 100, doi: [10.3847/1538-4357/aaff65](https://doi.org/10.3847/1538-4357/aaff65)
- Debras, J., Chabrier, G., & Stevenson, D. J. 2021, *Astrop. J. Lett.*, 913, 21
- Duarte, L. D. V., Wicht, J., & Gastine, T. 2018, *Icarus*, 299, 206
- Durante, D., Buccino, D. R., Tommei, G., et al. 2020, *Geophys. Res. Lett.*, 47, e2019GL086572
- Fuller, J. 2014, *Icarus*, 242, 283–296
- Galanti, E., & Kaspi, Y. 2021, *MNRAS*, 501, 2352–2362
- Gonzalez-Cataldo, F., Wilson, H. F., & Militzer, B. 2014, *Astrophys. J.*, 787, 79
- Goodman, J., & Weare, J. 2010, *Communications in Applied Mathematics and Computational Science*, 5, 65, doi: [10.2140/camcos.2010.5.65](https://doi.org/10.2140/camcos.2010.5.65)
- Guillot, T. 1999, *Planet. Space Sci.*, 47, 1183, doi: [10.1016/S0032-0633\(99\)00043-4](https://doi.org/10.1016/S0032-0633(99)00043-4)
- Guillot, T., Miguel, Y., Militzer, B., et al. 2018, *Nature*, 555, doi: [10.1038/nature25775](https://doi.org/10.1038/nature25775)
- Hubbard, W. B. 1974, *Icarus*, 21, 157
- . 2013, *Astrophys. J.*, 768, 43, doi: [10.1088/0004-637X/768/1/43](https://doi.org/10.1088/0004-637X/768/1/43)
- Hubbard, W. B., & Militzer, B. 2016, *Astrophys. J.*, 820, 80
- Idini, B., & Stevenson, D. J. 2022, *The Planetary Science Journal*, 3, 89, doi: [10.3847/psj/ac6179](https://doi.org/10.3847/psj/ac6179)
- Jones, C. A. 2014, *Icarus*, 241, 148–159
- Kaspi, Y., Davighi, J. E., Galanti, E., & Hubbard, W. B. 2016, *Icarus*, 276, 170
- Kaspi, Y., & Galanti, E. 2016, *Astrophys. J.*, 820, 91
- Kaspi, Y., Galanti, E., Showman, A. P., et al. 2020, *Space Science Reviews*, 216, 84, doi: [10.1007/s11214-020-00705-7](https://doi.org/10.1007/s11214-020-00705-7)
- Kaspi, Y., Galanti, E., Hubbard, W., et al. 2018, *Nature*, 555, doi: [10.1038/nature25793](https://doi.org/10.1038/nature25793)
- Leconte, J., & Chabrier, G. 2013, *Nat. Geosci.*, 6, 347, doi: [10.1038/ngeo1791](https://doi.org/10.1038/ngeo1791)
- Ledoux, P. 1947, *Astrophys. J. Lett.*, 105, 305
- Li, C., Ingersoll, A., Bolton, S., et al. 2020, *Nature Astronomy*, 4, 609, doi: [10.1038/s41550-020-1009-3](https://doi.org/10.1038/s41550-020-1009-3)
- Lindal, G. F., Wood, G. E., Levy, G. S., et al. 1981, *Journal of Geophysical Research: Space Physics*, 86, 8721, doi: [10.1029/JA086iA10p08721](https://doi.org/10.1029/JA086iA10p08721)
- Liu, S.-F., Hori, Y., Muller, S., et al. 2019, *Nature*, 572, 355
- Lodders, K. 2010, in *Astrophysics and Space Science Proceedings*, ed. A. Goswami & B. E. Reddy (Berlin: Springer-Verlag), 379–417
- Mahaffy, P. R., Niemann, H. B., Alpert, A., et al. 2000, *J. Geophys. Res.*, 105, 15061
- Mathworks. 2022
- Miguel, Y., Bazot, M., Guillot, T., et al. 2022, *Astron. and Astrophys.*, 662, A18
- Militzer, B. 2013, *Phys. Rev. B*, 87, 014202
- Militzer, B., & Hubbard, W. B. 2013, *Astrophys. J.*, 774, 148
- Militzer, B., Wahl, S., & Hubbard, W. B. 2019, *The Astrophysical Journal*, 879, 78, doi: [10.3847/1538-4357/ab23f0](https://doi.org/10.3847/1538-4357/ab23f0)
- Moll, R., Garaud, P., Mankovich, C., & Fortney, J. J. 2017, *ApJ*, 849, 24, doi: [10.3847/1538-4357/aa8d74](https://doi.org/10.3847/1538-4357/aa8d74)
- Moore, K. M., Yadav, R. K., Kulowski, L., et al. 2018, *Nature*, 561, 76, doi: [10.1038/s41586-018-0468-5](https://doi.org/10.1038/s41586-018-0468-5)
- Morales, M. A., McMahon, J. M., Pierleone, C., & Ceperley, D. M. 2013, *Phys. Rev. Lett.*, 110, 065702
- Müller, S., Helled, R., & Cumming, A. 2020, *Astronomy and Astrophysics*, 638, id.A121
- Nettelmann, N., Becker, A., Holst, B., & Redmer, R. 2012, *Astrophys. J.*, 750, 52
- Nettelmann, N., Movshovitz, N., Ni, D., et al. 2021, *Planetary Science Journal*, 2, 241, doi: [10.3847/psj/ac390a](https://doi.org/10.3847/psj/ac390a)
- Press, W. H., Teukolsky, S. A., Vetterling, W. T., & Flannery, B. P. 2001, *Numerical Recipes in C++* (Cambridge, UK: Cambridge University Press)
- Roulston, M., & Stevenson, D. 1995, *EOS*, 76, 59–72
- Saumon, D., Chabrier, G., & Horn, H. M. V. 1995, *Astrophys. J. Suppl.*, 99, 713
- Seiff, A., Kirk, D. B., Knight, T. C. D., et al. 1997, *Science*, 276, 102, doi: [10.1126/science.276.5309.102](https://doi.org/10.1126/science.276.5309.102)
- Soubiran, F., & Militzer, B. 2015, *Astrophys. J.*, 806, 228
- Stevenson, D., & Salpeter, E. 1977, *Astrophys. J. Suppl.*, 35, 239
- Tollefson, J., Wong, M. H., de Pater, I., et al. 2017, *Icarus*, 296, 163, doi: <https://doi.org/10.1016/j.icarus.2017.06.007>
- Vazan, A., Helled, R., & Guillot, T. 2018, *Astronomy and Astrophysics*, 610, id.L14
- von Zahn, U., Hunten, D. M., & Lehmacher, G. 1998, *J. Geophys. Res.*, 103, 22815
- Wahl, S. M., Wilson, H. F., & Militzer, B. 2013, *Astrophys. J.*, 773, 95
- Wahl, S. M., Hubbard, W. B., Militzer, B., et al. 2017, *Geophys. Res. Lett.*, 44, 4649, doi: [10.1002/2017GL073160](https://doi.org/10.1002/2017GL073160)

- 503 Wilson, H. F., & Militzer, B. 2010, Phys. Rev. Lett., 104,
504 121101. <http://www.ncbi.nlm.nih.gov/pubmed/20366523>
- 505 —. 2012a, Phys. Rev. Lett., 108, 111101,
506 doi: [10.1103/PhysRevLett.108.111101](https://doi.org/10.1103/PhysRevLett.108.111101)
- 507 —. 2012b, Astrophys. J., 745, 54,
508 doi: [10.1088/0004-637X/745/1/54](https://doi.org/10.1088/0004-637X/745/1/54)
- 509 Wong, M., Mahaffy, P. R., Atreya, S. K., Niemann, H. B.,
510 & Owen, T. C. 2004, Icarus, 171, 153